applied sciences

MDPI

Article

New Insight into the Interfacial Transition Zone in Concrete Based on Fluorescence Microscopy

Jiarong Shen [1,2], Pengxiang Qin [2,*] and Yunke Wang [3]

[1] School of Future Cities, University of Science and Technology Beijing, Beijing 100083, China; jiarongshen@ustb.edu.cn
[2] State Key Laboratory of Hydroscience and Engineering, Tsinghua University, Beijing 100084, China
[3] Sichuan Huaneng Kangding Hydropower Co., Ltd., Kangding 610041, China; ww317612240@163.com
* Correspondence: pengxiangqinthu@126.com

Abstract

The interfacial transition zone (ITZ) in the aggregate periphery is often regarded as the weakest area in concrete. In this study, the results of extensive image analysis provide a new insight. First, fluorescence microscopy (FM) was adopted to obtain the microstructure of "complete ITZ", which overcomes several limitations of the scanning electron microscope method. Then, an ITZ recognition interactive algorithm was proposed, which quantitatively characterizes the pore distributions in the ITZ and cement paste in both lateral and longitudinal directions. Finally, based on the experimental and statistical results, the pore distributions around aggregates, coarse sand and fine sand were characterized. Along the lateral direction, a high non-uniformity was observed in the porosity between units, taken at the same distance from the aggregate/sand surface. On the contrary, along the longitudinal direction, statistical results show minimal increases in the porosity within the ITZ. This is also applicable even in the innermost ITZs.

Keywords: concrete; interfacial transition zone (ITZ); fluorescence microscopy (FM); porosity distribution; image analysis

1. Introduction

Concrete is a composite construction material composed of coarse and fine aggregates bonded together by a cementitious matrix. The microstructure and composition of hydrated cement paste in the vicinity of aggregate particles differ from those of bulk cement paste, and this region is commonly known as the interfacial transition zone (ITZ). This concept has been widely recognized in the field of concrete science and engineering. Typically, the ITZ extends approximately 30–70 μm from the aggregate surface, and its microstructural characteristics are distinct from those of the bulk cement paste in conventional concrete [1–3]. Its microstructure is governed by several mechanisms, including the wall effect, gel syneresis, unidirectional hydration, micro-bleeding, and the formation of water films [1,4,5]. The ITZ is often regarded as the weakest component in concrete, as its higher porosity can facilitate the penetration of harmful substances [6,7] and acts as a favorable path for crack propagation [8–14]. To accurately describe the ITZ microstructure and forecast the macroscopic performance of conventional concrete, three-phase concrete models that account for the influence of the ITZ have been extensively applied in various numerical investigations of concrete [15–18].

The interfacial transition zone exerts a considerable influence on the macroscopic mechanical and physical properties of concrete. For this reason, many investigators have

Check for updates

Academic Editors: Sebastiano Candamano and Paulo Santos

Received: 16 March 2026
Revised: 17 April 2026
Accepted: 1 June 2026
Published: 25 June 2026

Copyright: © 2026 by the authors. Licensee MDPI, Basel, Switzerland. This article is an open access article distributed under the terms and conditions of the Creative Commons Attribution (CC BY) license.

concentrated on exploring the microstructural features of the ITZ and have aimed to achieve its quantitative description. In 1989, Scrivener [19] originally developed the "strip method", which enables quantitative evaluation of the ITZ microstructure. Using backscattered electron (BSE) imaging analysis, the ITZ region surrounding aggregate particles can be divided into a series of narrow strips whose boundaries run parallel to the aggregate surface. By performing grayscale-based statistical analysis, the porosity within each strip can be evaluated, yielding a curve that illustrates how porosity varies with increasing distance from the aggregate interface. Diamond [20,21] later refined this strip method in detail, suggesting that the ideal strip dimensions are approximately 170–200 μm in length and 5–10 μm in width. Scrivener [22] also established a quantitative framework for BSE images that can be effectively used to characterize the ITZ microstructure. As digital image processing techniques have advanced, numerous studies have analyzed ITZ characteristics using SEM/BSE image analysis [23–26]. For reference, Figure 1 displays a typical SEM backscattered micrograph obtained at a distance of roughly 30 μm from the aggregate surface [21]. The magnification for Figure 1 was 500 and the pixel resolution was 512 × 512. Due to technical limits of the equipment, each strip was only approximately 250 μm long. Therefore, the "complete ITZ" microstructure characteristics around aggregates/sands cannot be reflected. In addition, using SEM/BSE is time-consuming when a large number of ITZ images need to be investigated.

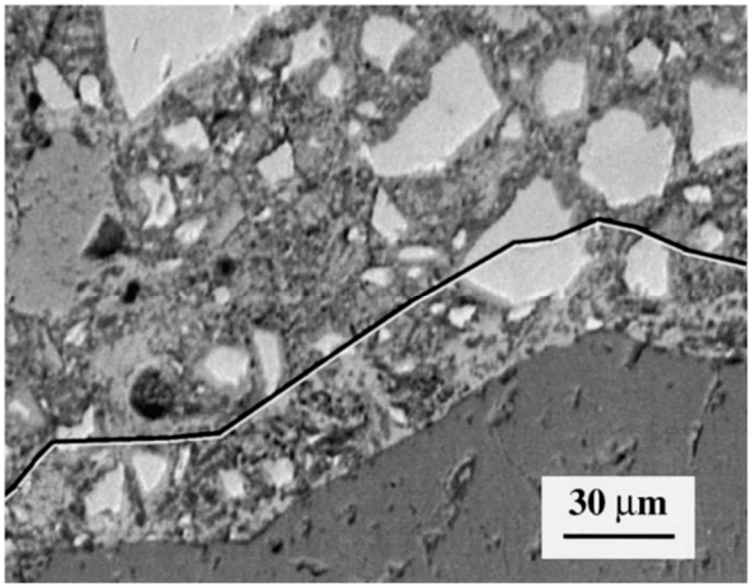


Figure 1. Backscattered SEM image of the ITZ (obtained from [21]).

Numerous ITZ models have been proposed for this purpose. A very high porosity is often assumed in the innermost strip of the ITZ [27–30] based on extensive SEM/BSE observations. Ollivier [27] observed an increasing porosity within the ITZ, with reported porosities of 30% or more within the innermost strip (0–5 μm). Scrivener [28] investigated the relationship between porosity and the distance to the aggregate surface of concrete of various ages. The experimental results showed that the ITZ porosity was 40% higher than that of the cement paste upon mixing. The porosity differences between the ITZ and the cement paste were reduced to 10–20% after one day. After a long period, the ITZ porosity was reduced by approximately the same amount as it is reduced in cement paste. Jia [29] tested the relationship between the detectable porosity of the ITZ around aggregates of various sizes and the distance to the aggregate surface. The results showed that the largest porosity differences decreased gradually (45% to 15%) with a decrease in aggregate size. However, the porosity within the innermost strip (0–10 μm) remained high, at more than

25% even for the ITZ around the smallest aggregate tested. Newman [30] suggested that the ITZ has a much higher porosity (2–3 times) than that of hardened cement paste farthest from the aggregate particles.

However, despite the commonly reported high porosity values in existing publications, a range of differing perspectives on porosity distribution within the ITZ have emerged based on comprehensive experimental data. Diamond [20,21] analyzed more than 6000 independent binary segmentations of the ITZ via SEM imaging and observed that the rise in porosity within the ITZ was relatively small. In fully hydrated concrete cured for 100 days, even the innermost strip, ranging from 0 to 10 μm from the aggregate, exhibited a porosity below 10%. The maximum difference in porosity across the ITZ was only about 4%. Rangaraju [31] prepared conventional concrete mixtures with varied fine aggregate gradings to systematically adjust the overall ITZ volume fraction, then conducted mechanical and permeability tests. The results demonstrated that compressive strength, splitting tensile strength, dynamic elastic modulus, and rapid chloride ion permeability were not significantly influenced by changes in ITZ content. Based on these findings, Rangaraju [31] argued that the traditional understanding of how the ITZ affects the macroscopic performance of ordinary concrete may be misleading. As a result, the validity of regarding the ITZ as an independent mechanical phase deserves further investigation.

In summary, despite the extensive studies on the microstructural characteristics of the ITZ and their effects on the macro properties of concrete, the understanding of the pore distribution within the ITZ and its effect on the macro properties of concrete is still inadequate. The heterogeneous distributions of porosity within the ITZ might not be described very well by SEM/BSE because of limited observation scale. The microstructural characteristics of the "complete ITZ" around aggregates/sands could not be reflected.

In view of the foregoing problems, experimental characterization of the microstructure of the ITZ was conducted in this study. First, FM observation [32–36] was utilized, instead of SEM, to obtain a sufficient number of "complete ITZ" images. Thus, the evolution of pore distribution in both ITZ and cement paste can be fully characterized. Next, an interactive algorithm of ITZ recognition, which can precisely distinguish and characterize the pore evolution characteristics of ITZ and cement paste, was proposed. Finally, the complex microstructural characteristics of the ITZ were analyzed based on the FM experimental results and interactive algorithm statistical results. The mechanism of the interactions between aggregates/sands and cement paste can thus be better understood.

2. Experimental Details

2.1. Material and Mix Designs

Medium-heat Portland cement P. MH42.5 with a density of 3230 kg/m^3 was used in this study. The chemical composition and properties of cement are as follows, in weight percentage: CaO, 47.87%; SiO_2, 25.12%; Al_2O_3, 11.29%; MgO, 5.52%; SO_3, 2.95%; Fe_2O_3, 2.39%; Na_2O, 0.65%; K_2O, 0.60%. Loss on ignition (LOI) was 2.63% and the remaining percentage corresponds to trace components or rounding. The coarse aggregate was crushed granite with a maximum particle size of 20 mm. The fine aggregate was natural river sand with a fineness modulus of 2.8. Table 1 lists the details of the concrete mix design. Supplementary cementitious materials, like fly ash and silica fumes, were not used in this study.

Table 1. Concrete mix design.

Constituent	OPC 42.5R	Coarse Aggregate	River Sand	Water
Proportion (kg/m^3)	416	1070	602	208

The concrete was poured into 100 mm × 100 mm × 100 mm cubical molds. The concrete was demolded after 1 day and cured in a standard curing room for one year. After curing, slices of 100 mm × 25 mm × 10 mm were cut from the middle part of the concrete samples, as presented in Figure 2. The observed areas in this study were 100 mm × 25 mm on the surface marked in pink in Figure 2 (right).

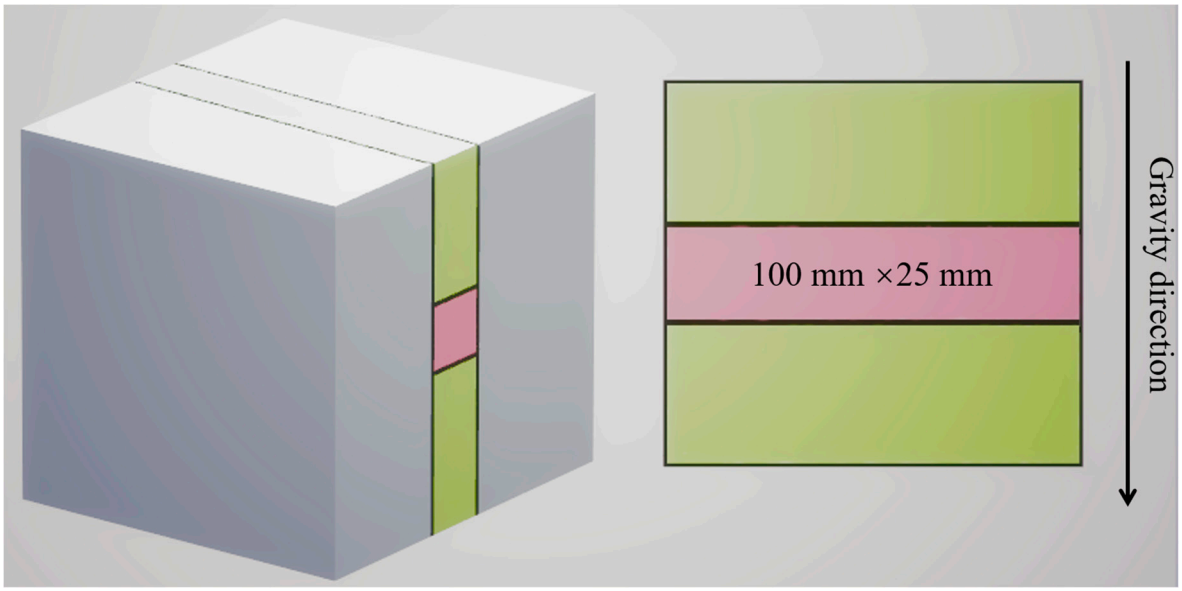


Figure 2. Cutting process of 100 mm × 25 mm × 10 mm slice.

2.2. FM Tests

In order to overcome the deficiency of the traditional SEM/BSE method [32–37], the FM test [38–42] was adopted to obtain a sufficient number of "complete ITZ" images. A "complete ITZ" is illustrated in Figure 3.

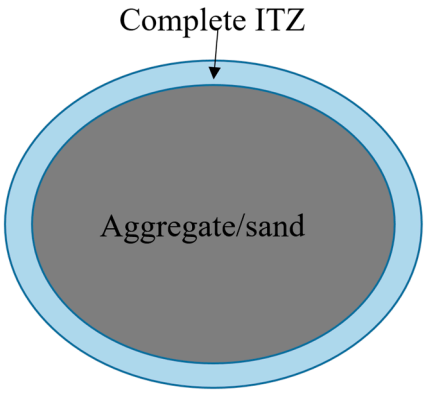


Figure 3. Diagram of "complete ITZ".

The experimental procedure of the FM test [43–45] is presented below. First, the prepared concrete specimens (10 mm × 100 mm × 25 mm) were ground with abrasive paper SiC p500 (70 μm), p800 (30 μm), p1000 (22 μm), and p1200 (15 μm). Then, they were polished using a grinder to obtain a smooth flat surface. The flat surfaces were cleaned to remove any leftover debris. After the above process, the specimens were dried in an oven at a temperature of 40 °C to prevent cracking [46]. After they were completely dry, the specimens were placed into a vacuum chamber at a constant pressure of 1 kPa and then impregnated with fluorescent resin while maintaining the vacuum. In this study, epoxy resin with 380 cP viscosity was proved to be generally satisfactory for specimen preparation

and could provide reliable impregnations [47]. Finally, the 100 mm × 25 mm surfaces of the prepared specimens were observed under a fluorescent microscope system (presented in Figure 4) to store the images for further processing and analysis.

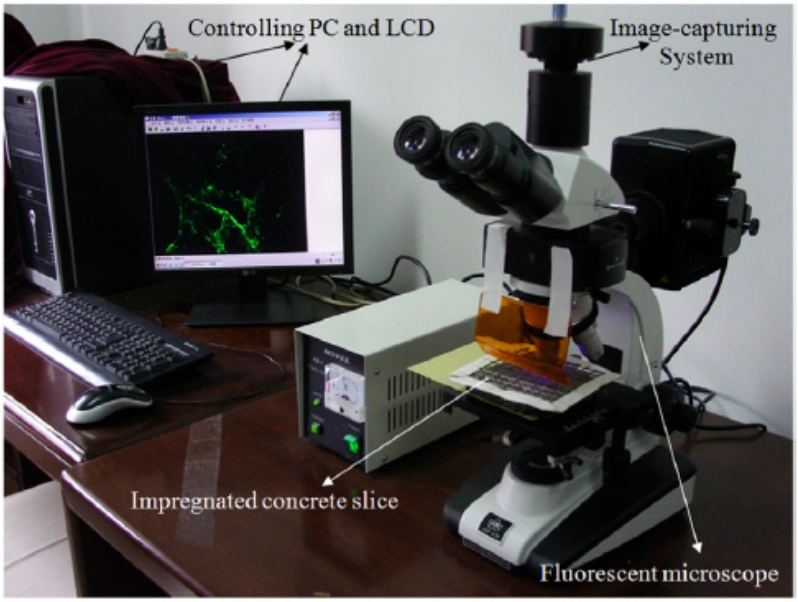


Figure 4. The fluorescent microscope system [38].

During observation, the concrete specimens were scanned grid by grid on the stage. The pixel size was 2 μm. Each local unit image covers an area of 2.784 × 2.080 mm (1392 × 1040 pixels), as shown in Figure 5. Consequently, the global image (100 mm × 25 mm) of each specimen was composed of 432 local unit images: 36 local unit images along the width direction and 12 local unit images in the length direction. The fluorescence area in Figure 5 represents the defects in the concrete. The whole image of the tested impregnated concrete specimen can be obtained by utilizing all local unit images through an image mosaic algorithm [48]. The whole image is not provided here due to its large size.

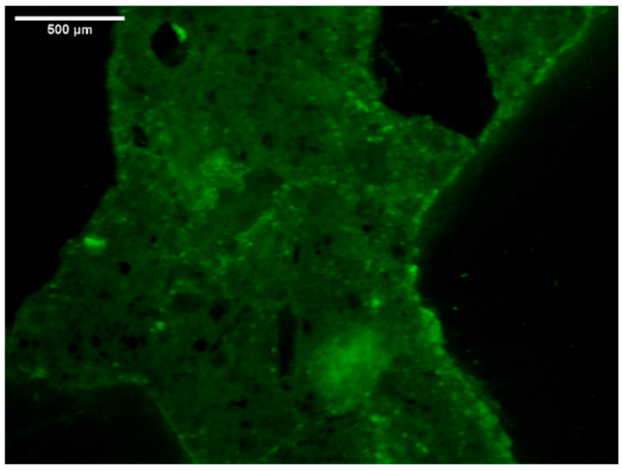
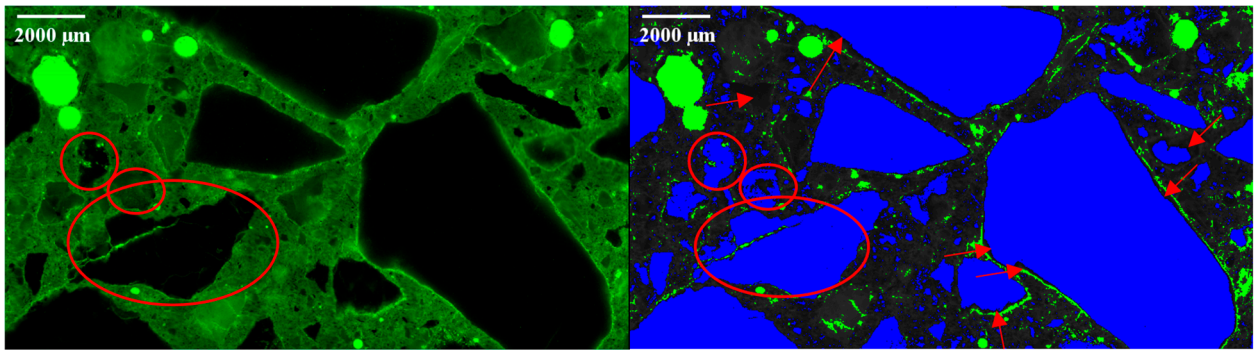


Figure 5. Local unit image of concrete specimen by FM tests (2.784 mm × 2.080 mm).

3. Interactive Algorithm of ITZ Recognition

Setting the threshold between aggregate or sand particles and cement paste is a critical step in edge detection, and this process inevitably influences the accuracy of ITZ identification. In conventional global thresholding and adaptive threshold segmentation methods, the entire image is segmented automatically using either a single global threshold or an

adaptive threshold matrix. However, during fluorescence microscopy (FM) testing, the threshold contrast between individual aggregate or sand particles and the surrounding cement paste varies slightly due to the effects of epoxy impregnation and the surface characteristics of the concrete specimen, as illustrated in Figure 6a. As seen in the segmentation outcomes obtained using traditional thresholding approaches (Figure 6b), such minor variations in threshold levels can result in imprecise edge extraction, as indicated by the red arrows. Therefore, in concrete FM micrographs, the threshold separating each aggregate or sand particle from the cement paste is not uniform and cannot be adequately represented by either a global threshold or an adaptive threshold matrix. Furthermore, traditional threshold-based segmentation relies solely on grayscale intensity and ignores the inherent morphological features of the image. As highlighted by the red circles in Figure 6b, the boundaries of certain aggregate or sand particles remain unclosed, which deviates from actual physical conditions. Consequently, the area and perimeter of the corresponding particles cannot be accurately computed.



(**a**) (**b**)

Figure 6. Segmented results using traditional threshold algorithms. (**a**) Original FM image; (**b**) segmented image.

Therefore, traditional threshold algorithms are not fully applicable to the segmentation of concrete FM images. In order to make up for the deficiency of traditional algorithms, an interactive algorithm, which can accurately segment the edges of the aggregate/sand, is proposed in this study.

3.1. Edge Extraction of Aggregate/Sand

To process and define the threshold between aggregate/sand and cement paste, the source FM images were first converted into gray images. Then, a graphical user interface (GUI) was designed to select the gray threshold (0–255) to split the aggregate/sand and cement paste. During the interactive process, the user first selects any aggregate/sand to observe. Subsequently, a tracking bar is activated for threshold selection. The connected regions composed of the aggregate/sand position and threshold are extracted. The above steps are repeated until the precise edges of the selected aggregate/sand and all other aggregates/sands have been extracted. For the sake of simplicity, only the edge extraction result of a representative aggregate is presented in Figure 7.

Compared with the traditional global threshold and adaptive threshold segmentation algorithms, the interactive algorithm sets the corresponding threshold for each aggregate/sand edge, which will ensure the identification accuracy. The effect of threshold difference between each aggregate/sand edge is taken into full consideration. Furthermore, after the interactive algorithm, the whole FM images can be clearly divided into aggregate, sand, and cement paste. The area and perimeter data of corresponding aggregates/sands can be easily obtained. The characteristics of image itself can also be investigated.

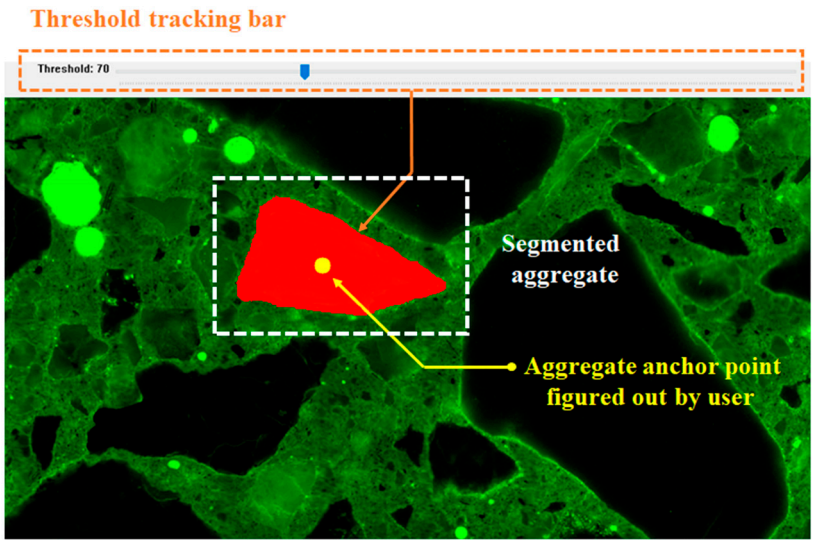


Figure 7. Representative aggregate segmentation through GUI.

3.2. Successive Strip/Unit Extraction

After precise edges of all representative aggregates/sands have been extracted, the ITZ areas around those aggregates/sands can be further investigated. An 8-connected kernel was applied to extend the edge of the aggregate/sand area. Ten successive strips were extracted for analysis. The width of each narrow strip was set as 20 μm after a comprehensive consideration of the image resolution and study area. Furthermore, to further investigate the pore distributions along the aggregate–sand surface direction, a GUI was designed to split the ITZ area. The number of units to be split can be set by users. The successive strip/unit extraction result of the representative aggregate is shown in Figure 8.

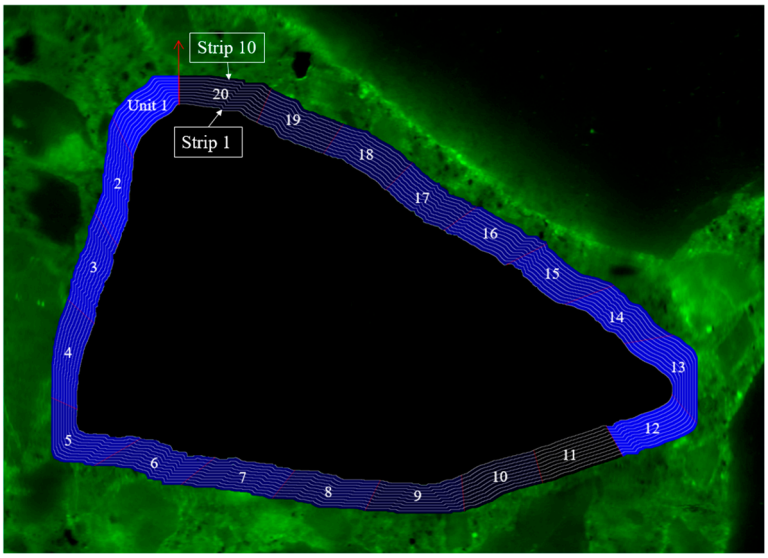


Figure 8. Result of successive strip/unit extraction for the representative aggregate (the split unit number is set to 20).

3.3. Pore Threshold Selection Within Strips/Units

To evaluate the average percentage area of detectable pores within each strip/unit, another threshold, which splits the cement paste and pores, was selected by the GUI. After the extraction of successive strip/unit steps presented in Section 3.2, a tracking bar was activated for threshold selection. Through repeatable threshold adjustment, a threshold value that accurately distinguishes pores and cement paste could eventually be selected.

The threshold value is obtained as follows: First, select three typical pores in the FM image for analysis. Then, measure the area of each selected pore and select a threshold value and measure the corresponding area of each pore. Finally, compare the areas of the original FM image and the image after a threshold setting. If the areas considerably differ, reset the threshold value until the difference is less than 1%. After finishing the setting, the white parts in Figure 9 represent the pore distributions within all strips of (0–200 μm)/units.

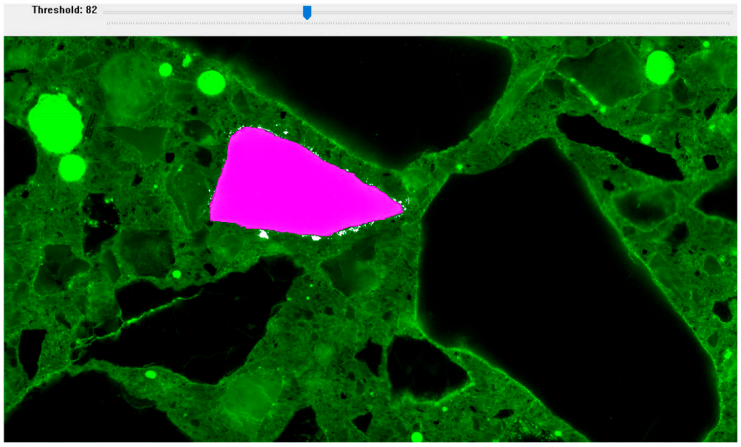


Figure 9. Pore distributions within all strips/units.

3.4. Statistical Analysis

To better evaluate the ITZ microstructure characteristics statistically, the areas of selected aggregate/sand and pores within each strip and each unit were calculated using the number of pixels and saved automatically as a CSV file using the proposed ITZ recognition interactive algorithm. In addition, the pore distribution images of each unit were extracted to facilitate further investigations (Figure 10).

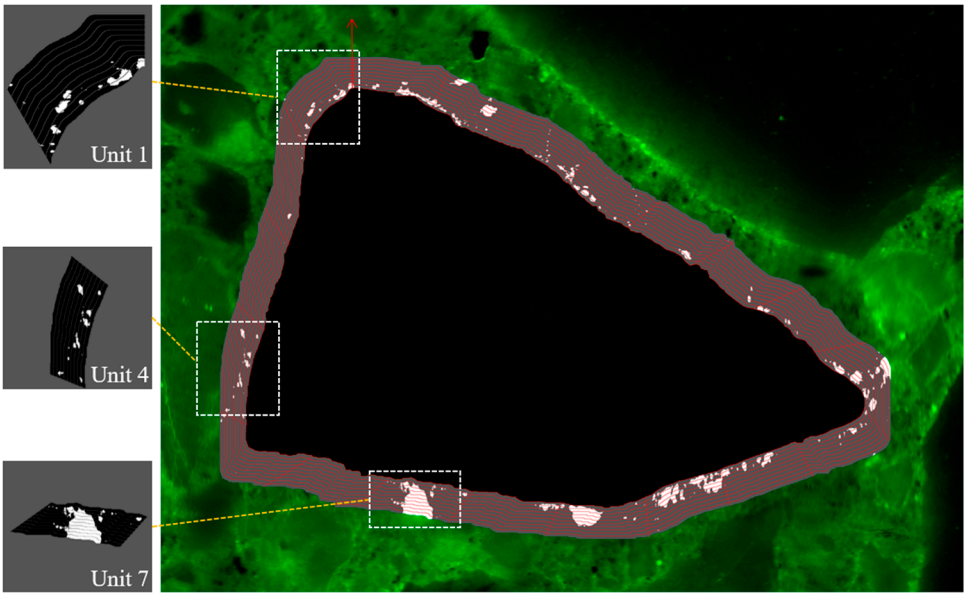


Figure 10. Pore distribution images around the representative aggregate.

Based on the FM test results and the proposed ITZ recognition interactive algorithm, the pore distributions around 691 aggregates, 556 coarse sand particles, and 343 fine sand particles were extracted for statistical analysis. For comparison, 675 cement paste units were also analyzed.

Considering that the aggregate/sand areas in the two-dimensional section may be smaller than that in the three-dimensional section, the threshold area between aggregates and sand particles may decrease concomitantly. After repeated observations, 4 mm^2 was selected as the threshold area between the aggregate and sand. Similarly, the threshold area between coarse sand and fine sand was selected as 0.1 mm^2. The 675 cement paste units were randomly selected using a circular frame with a 20 μm semi-diameter. To avoid the effect of ITZ, the selected cement paste units are all more than 200 μm off the surface of aggregate/sand. Table 2 presents the classification criteria of the aggregate, sand, and cement paste.

Table 2. Classification criteria of aggregate and sand.

Type of Inclusions	Area (mm^2)	Number of Samples
Aggregate	>4	691
Coarse sand (0.1 mm^2–2 mm^2)	0.1–4	556
Fine sand (<0.1 mm^2)	<0.1	343
Cement paste	-	675

4. Results and Discussion

4.1. Assessment of Pore Size Distributions of ITZ and Cement Paste

It is generally accepted that the microstructure of the ITZ, generally extending 30–70 μm from the aggregate surface, differs from that of cement paste in ordinary concrete. To investigate the pore distribution differences of the ITZ and cement paste in both lateral (parallel to aggregate/sand surface) and longitudinal (perpendicular to aggregate/sand surface) directions, porosity values for a full set of 20 units, which entirely surround the representative aggregate in an anticlockwise direction, are presented in Table 3. Strips, whose contours are parallel to the surface of the aggregate, are numbered in sequence according to the distance away from the aggregate surface (strip 1: 0–20 μm, strip 2: 20–40 μm, . . ., strip 10: 180–200 μm). The pore distribution around the representative aggregate is shown in Figure 11 and Table 3.

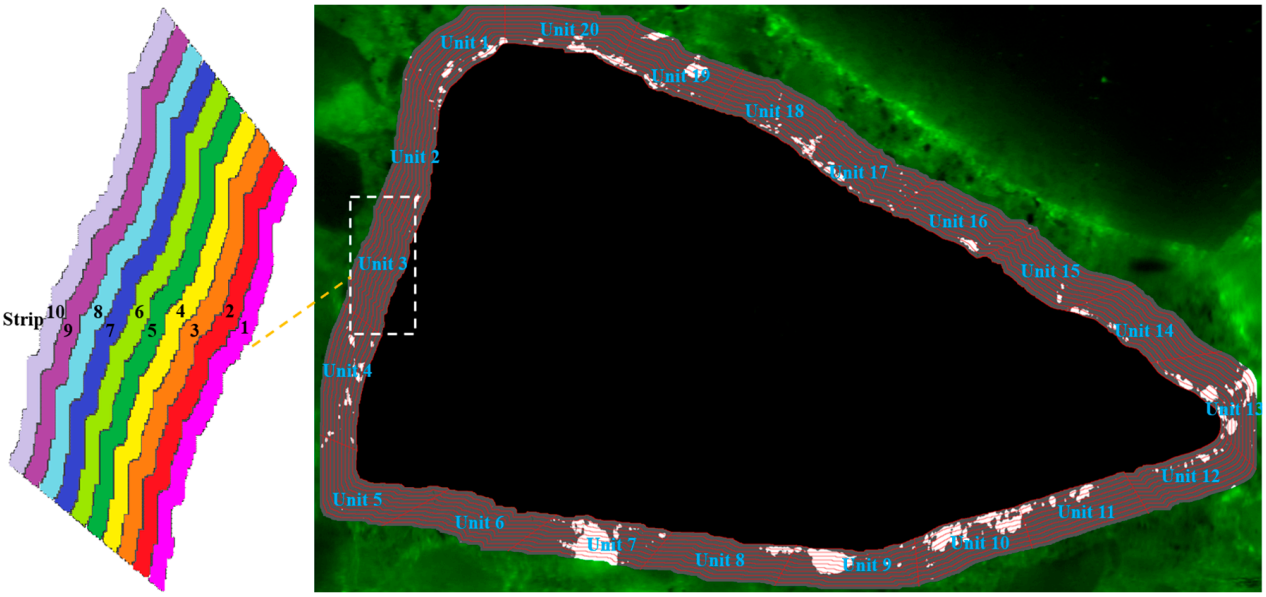


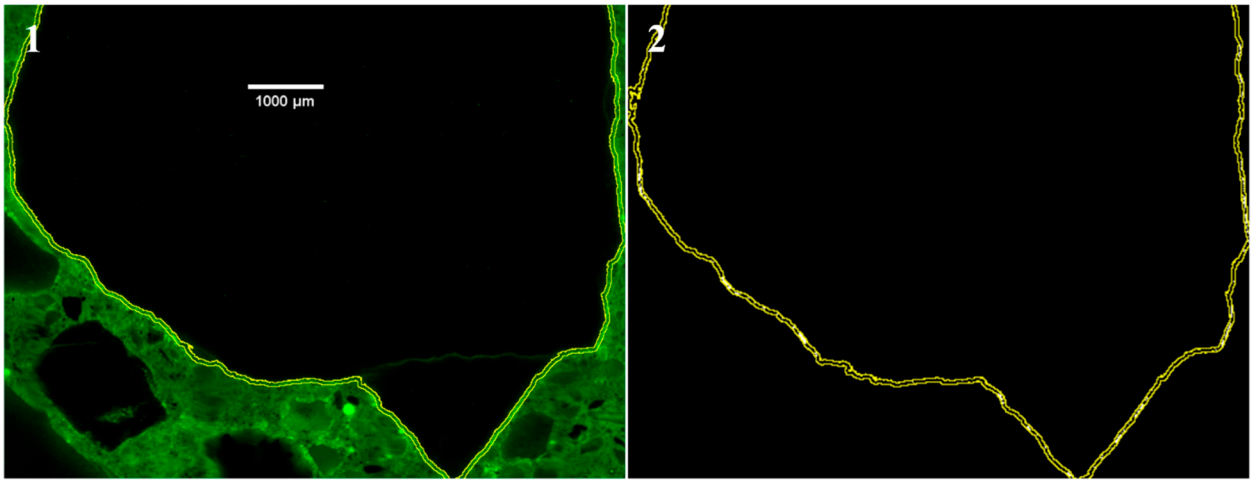
Figure 11. Pore distribution results surrounded the representative aggregate.

Table 3. Porosity values found in strips surrounding a representative aggregate.

Unit No.	Porosity (%)										
	Strip 1	**Strip 2**	**Strip 3**	**Strip 4**	**Strip 5**	**Strip 6**	**Strip 7**	**Strip 8**	**Strip 9**	**Strip 10**	**AVG**
1	17.87	18.59	10.97	4.63	0.03	0.00	0.13	0.23	0.00	0.57	5.30
2	0.59	0.13	4.27	0.00	0.00	0.00	0.00	0.00	0.07	0.22	0.53
3	0.00	0.05	0.00	0.00	0.00	0.00	0.00	0.00	0.00	0.00	0.01
4	1.77	12.59	7.90	5.78	2.74	5.73	1.88	1.76	0.00	0.00	4.01
5	0.00	0.00	0.00	0.00	0.00	0.00	0.00	0.33	1.10	1.06	0.25
6	0.00	0.00	0.00	0.00	0.00	0.00	0.00	0.00	0.00	0.00	0.00
7	1.56	21.38	22.34	24.40	22.11	24.48	27.30	35.73	32.38	32.33	24.40
8	6.44	14.80	3.27	0.00	0.00	0.00	0.00	0.00	0.00	0.00	2.45
9	15.45	31.62	29.93	30.67	26.74	16.70	2.24	0.00	0.00	0.00	15.34
10	27.38	48.59	48.15	47.41	27.52	4.04	0.92	0.00	0.00	0.35	20.43
11	15.03	31.18	12.78	1.04	0.10	0.00	0.00	0.00	0.00	0.00	6.01
12	1.43	8.20	10.30	0.08	0.57	0.00	0.00	0.00	0.00	1.01	2.16
13	27.06	31.63	18.82	9.60	6.97	1.40	7.08	10.08	18.11	21.60	15.24
14	13.10	6.90	0.00	0.00	0.00	0.00	0.00	0.00	0.00	0.00	2.00
15	0.00	1.71	3.77	0.00	1.66	0.05	0.00	0.00	0.00	0.00	0.72
16	4.26	13.79	0.92	0.05	0.00	0.00	0.00	0.02	0.00	0.10	1.91
17	14.43	20.14	4.18	0.00	0.16	0.03	0.96	0.05	0.57	0.17	4.07
18	3.51	13.44	7.11	4.48	1.63	1.30	0.23	0.30	0.02	0.05	3.21
19	14.25	10.56	0.39	0.00	0.05	11.76	14.94	11.94	8.89	11.46	8.42
20	26.10	27.80	4.20	3.64	0.93	0.00	0.00	0.00	0.00	0.00	6.27
AVG	9.51	15.66	9.46	6.59	4.56	3.27	2.78	3.02	3.06	3.45	5.39

AVG represents the average porosity.

To further investigate the lateral and longitudinal pore distribution within an ITZ, ITZs of three aggregates and three sand particles were randomly selected and presented in Figures 12 and 13, respectively. The figures on the left side are the original FM images. The part enclosed by the yellow lines is the ITZ area, whose width is set as 50 μm. The figures on the right side are the binary images corresponding to the left-side images. As presented in Figures 12 and 13, the "lower" part represents 0–25 μm from the aggregate/sand surface; the "upper" part is 25–50 μm from the aggregate/sand surface.



(**a**)

Figure 12. *Cont.*

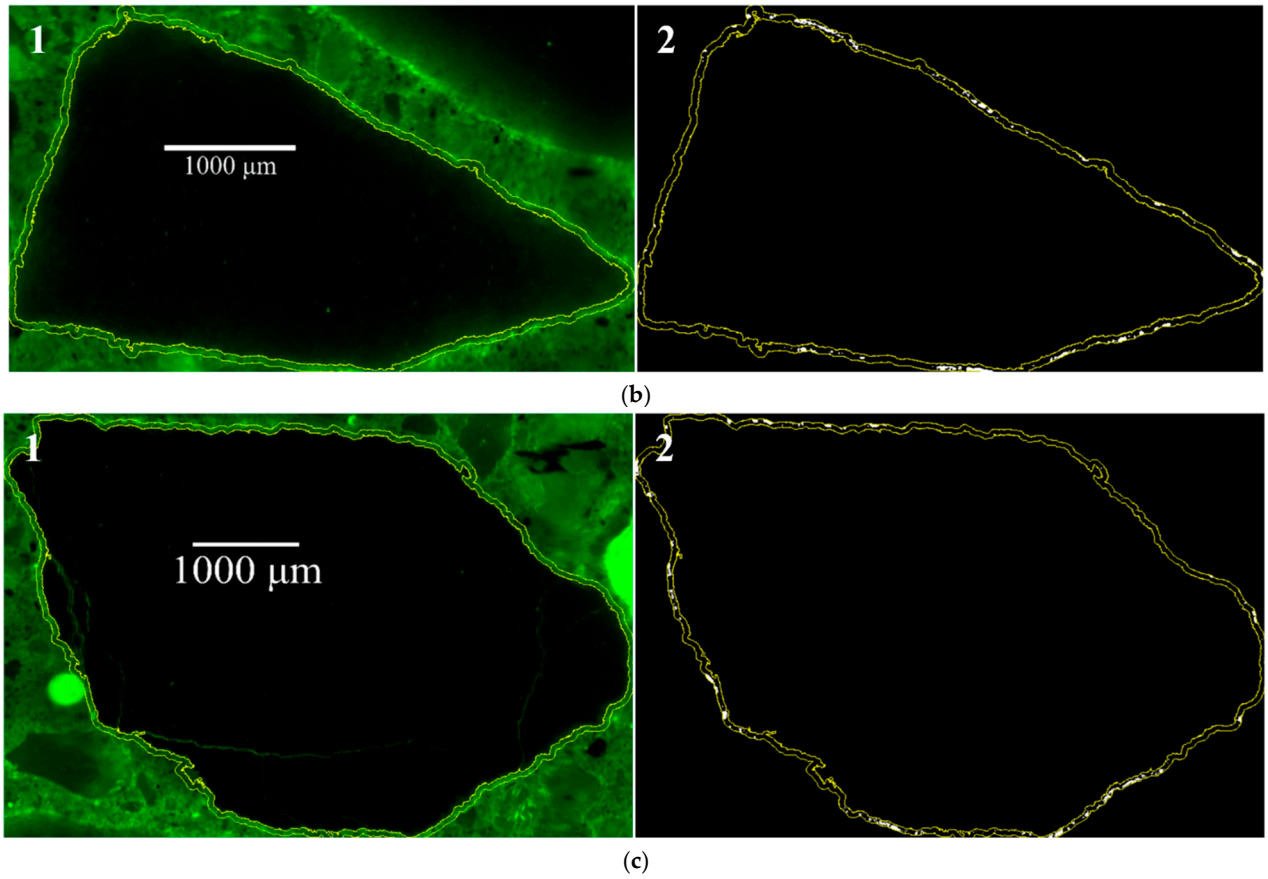


Figure 12. Aggregate ITZ strips: 1 Original FM image, and 2 Binary images. (**a**) Aggregate 1. (**b**) Aggregate 2. (**c**) Aggregate 3.

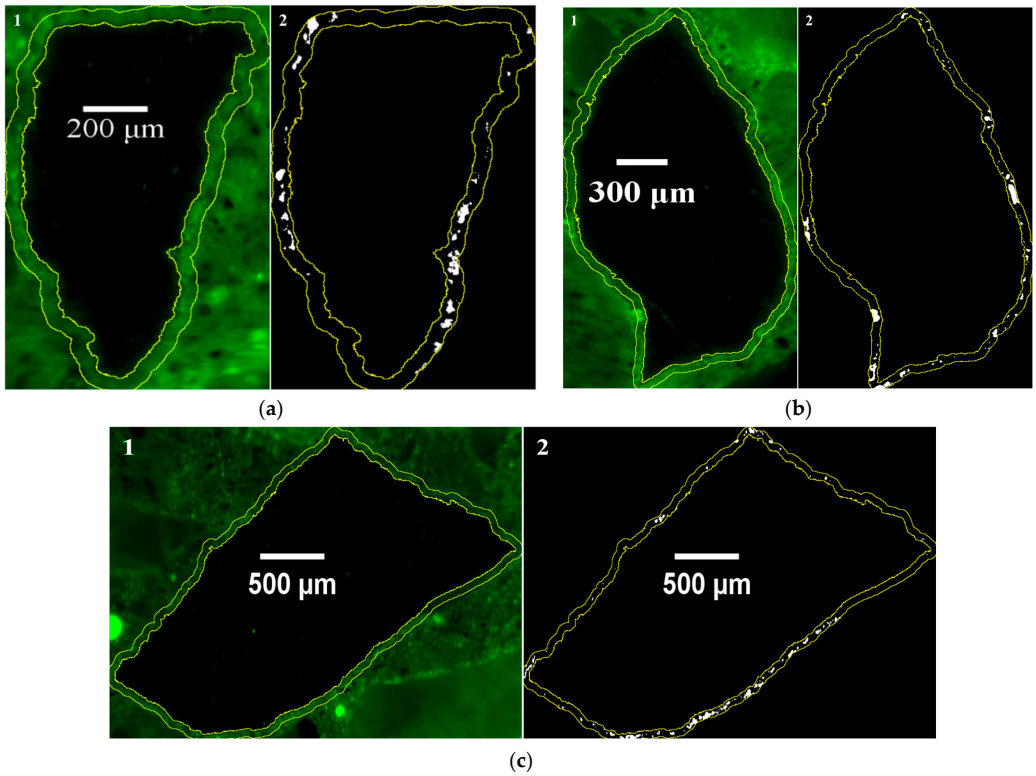


Figure 13. Sand ITZ strips: 1 Original FM image, and 2 Binary images. (**a**) Sand 1. (**b**) Sand 2. (**c**) Sand 3.

4.1.1. Lateral Pore Distribution Variation

As shown in Table 3, the average porosity within the first strip (0–20 μm) was measured as 9.51%. It can be clearly seen that the porosity of individual regions around the aggregate particles varies considerably. Among the 20 sampling units in the first strip, the porosity values ranged from 0.00% to 27.38%, with a standard deviation of 9.49 and a coefficient of variation close to 100%. This indicates a high degree of heterogeneity in the porosity distribution across the first strip. As presented in Table 3, comparable degrees of variation were also observed in the porosity values of the second and all subsequent strips. Accordingly, the locally high-porosity "local ITZ" regions obtained from SEM/BSE observations are not representative of the overall microstructural features of the "full ITZ" in concrete.

As shown in Figures 11–13, in both the ITZ and other cement paste areas, detectable pores were not homogeneously distributed. This phenomenon is observed in all figures. It is evident that there is a high degree of non-uniformity in the pore content. This also indicates the occurrence of clustering; that is, there are groups of pores. The pores within the other parts are fewer and even close to zero, except for the pore clusters. The pore clustering in some local areas and absence in other areas reflect a "patchy" characteristic, which has previously been found in cement paste in concrete [49].

4.1.2. Longitudinal Pore Distribution Variation

As presented in Table 3, in each unit, with the increase in distance from the aggregate/sand surface, the porosity varies significantly. The changes in porosity are irregular. However, from the overall perspective, the average porosity of each strip (entirely surround the representative aggregate) shows a decreasing trend with increasing distance. The porosity of the ITZ is slightly higher than that of cement paste.

To further investigate the longitudinal pore distribution of ITZ, the "lower" and "upper" parts presented in Figures 12 and 13 are compared. There is no indication of pores concentrating within the "lower" part. No significant differences are found in the area percentage of detectable pores in the "lower" and "upper" parts.

As presented in Table 3, after comparing the porosity of strip 1 (0–20 μm) and strip 2 (20–40 μm) in each unit, the highly enhanced porosity phenomenon within the innermost strip from the aggregate/sand surface was not found.

4.1.3. Discussion on Microstructure Characteristics of ITZ

In recent years, a large number of studies have examined ITZ microstructural images using the SEM/BSE technique. Because of the restricted field of view associated with SEM/BSE imaging, only local regions of the ITZ can be captured. As a result, micrographs of local ITZ regions showing exceptionally high porosity frequently appear in the published literature. This pattern may lead investigators to assume that the full ITZ possesses a microstructure similar to that of these small local zones. As a consequence, the overall porosity of the ITZ is at risk of being significantly overestimated.

As presented in Table 3, in the innermost strip (strip 1), the porosities of units 10, 13, and 20 are significantly higher than the average porosity. Oppositely, the porosities of units 2, 3, 4, 5, 6, 7, 12, 15, are no more than 2%. Therefore, the microstructure of a "complete ITZ" is different from that of a "local ITZ". Given the high variation between local units, it is apparent that the microstructure of the "local ITZ" obtained by the SEM/BSE method can neither describe the microstructure characteristics of the "complete ITZ" nor reflect the local variations between units around aggregates/sand particles.

4.2. Statistical Results of Pore Evolution Within the ITZ

As discussed in Section 4.1, a high degree of non-uniformity in the pore area percentage of units at the same distance from the same aggregate/sand was observed. The analysis of the ITZ of several aggregates/sands could not adequately describe the ITZ microstructure characteristics. Therefore, it is necessary to conduct a more in-depth statistical analysis of the porosity evolution within the ITZ.

As presented in Section 3.4, based on the ITZ recognition interactive algorithm proposed above, 1590 pieces of data for both the ITZ and cement paste were obtained (691 pieces around aggregates, 556 around coarse sand, and 343 around fine sand). Porosity values in the strips of 0–20 μm, 20–40 μm, 40–60 μm, 60–80 μm, 80–100 μm, 100–120 μm, 120–140 μm, 140–160 μm, 160–180 μm, and 180–200 μm, and the corresponding aggregate/sand area, were included in a dataset. In addition, the average porosity of the 675 randomly selected cement pastes was also calculated to provide a comparison for the ITZ analysis.

In Figure 14, the average porosities of the first strips (0–20 μm) around 691 aggregates, 556 coarse sand particles, and 343 fine sand particles are assigned to the first point of aggregate, coarse sand, and fine sand, respectively. The other points correspond to the average values of the second (20–40 μm), third (40–60 μm), and subsequent strips. The average porosity of 675 cement paste is presented as a red dotted line in Figure 14.

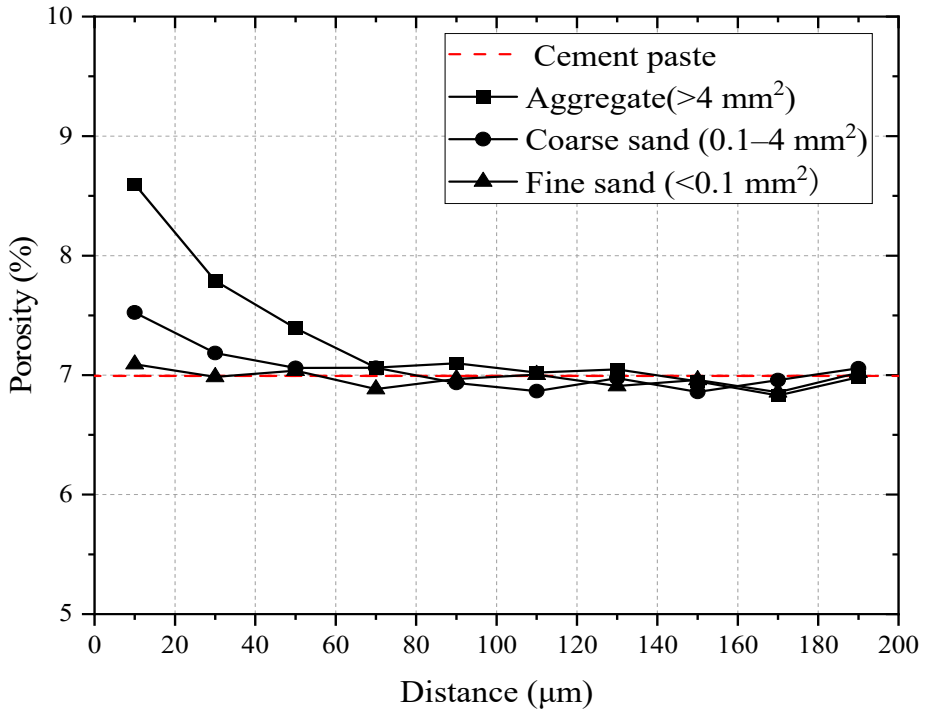


Figure 14. Porosity evolution of the ITZ.

As presented in Figure 14, a large gradient of increasing porosity within the ITZ reported by some researchers [27–30] is not found. Even the innermost strip shows porosities less than 9% for the ITZ around the aggregate. Moreover, the porosity is less than approximately 8% for the ITZ around coarse sand, compared with 30% or more reported in the literature. The largest differences between the average porosity of cement paste and innermost strip around aggregates and coarse sand are 1.60% and 0.53%, respectively. In addition, the average porosity of the ITZ around the aggregate and coarse sand first decreases and then remains with increasing distance from the aggregate/sand surface. The evolution of the average porosity in each strip with distance from the aggregate/sand surface is in

accordance with the conventional definition of the ITZ. However, the observations indicate that the porosity increase within the ITZ is minimal.

For the ITZ around the fine sand, the porosity remains unchanged with an increase in the distance from the surface. The porosity in all strips is close to the average porosity of the cement paste. Therefore, the ITZ around the fine sand exhibits essentially the same microstructure as the cement paste. The presence of fine sand may not affect the microstructure and pore distribution of the cement paste.

It can be also indicated in Figure 14 that the porosity of the innermost strip gradually decreases with a decrease in the inclusion size (aggregate–coarse sand–fine sand). The evolution trend of the porosities was also found in the second and third strips.

The porosities of the cement pastes and the innermost strips (0–20 μm) are compared in Table 4 and Figure 15. With the decrease in the inclusion size (aggregate–coarse sand–fine sand), both the porosity differences between the maximum and minimum values and the standard deviation decrease gradually. This indicates that the larger the inclusion size, the larger the porosity distribution dispersion.

Table 4. Comparison analysis of porosities between cement pastes and innermost strips.

Type of Inclusions	Average Porosity Within the Strip (0–20 μm) (%)			
	Average	Max	Min	Standard Deviation
Aggregate	8.60	12.87	6.02	1.95
Coarse sand	7.52	10.38	5.54	1.43
Fine sand	7.09	9.52	5.37	0.76
Cement paste	6.99	8.91	4.03	1.32

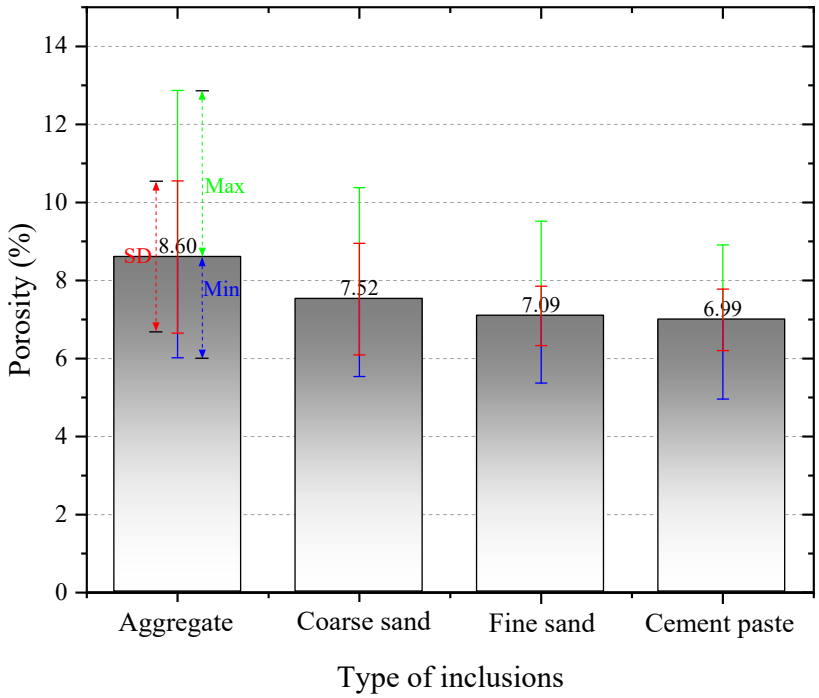


Figure 15. Comparison of porosities between cement pastes and innermost strips.

5. Discussion: Effects of ITZ on Macro Properties of Concrete

Extensive literature over the past 20 years has indicated that the ITZ is the weakest zone in concrete and the primary reason for the increase in permeability and decrease in strength. Concrete, a composite material, shows significant quasi-ductile behavior under compression loading. This differs from the brittle–elastic behavior of individual cement

pastes and aggregates. The well-known concrete behavior leads to the common view of ITZ being a weak link in concrete [28,50]. Accordingly, numerous aggregate–mortar–ITZ three-phase models [5,15–17,51,52] for concrete have been proposed. In these models, each component (aggregate, mortar, and ITZ) is treated as an individual unit with different properties. The "ITZ component" is assigned with significantly reduced properties.

Rangaraju [31] prepared concrete with different sand particle sizes (at a constant paste content) to test the effects of the ITZ extent on the macro properties of concrete. It was found that the measured "rapid chloride permeability," dynamic elastic modulus, and compressive strength of concrete were barely affected by variations in the ITZ contents. The results presented in this paper are in agreement with the findings of LeRoy [53].

In this study, based on the experimental and statistical results presented in Section 4, only small differences in the pore distribution between the ITZ around aggregates/sand and cement paste were observed. The average porosity within the ITZ, especially within the innermost strip, is only slightly higher than that of the cement paste. Therefore, the above considerations lead to the assumption that the ITZ around aggregate/sand in ordinary concrete may only have limited effects on the macro properties.

6. Conclusions

This study investigated the ITZ in concrete with a new insight by adopting the FM test, which can obtain a sufficient number of "complete ITZ" images. To further quantitatively investigate the pore distributions of both ITZ and cement paste, an ITZ recognition interactive algorithm was proposed. Based on the FM observations and the proposed interactive algorithm, statistical results of 691 pore distributions around aggregates, 556 around coarse sand particles, 343 around fine sand particles, and 675 within cement paste are analyzed. The microstructure characteristics of ITZ are hence understood from a different view. The following conclusions are drawn:

(1) An interactive algorithm of ITZ recognition has been proposed, which can quantitatively characterize the pore distributions of ITZ and cement paste in both lateral (parallel to aggregate/sand surface) and longitudinal (perpendicular to aggregate/sand surface) directions.

(2) The detectable pores were not homogeneously distributed throughout the ITZ. A high degree of non-uniformity was found in the porosity of each individual sampling unit taken at the innermost strip from the same aggregate. Similar variations were also observed in the corresponding percentage areas of detectable pores in the second and all subsequent strips. Consequently, given the high variation between local units, it is apparent that the microstructure of the "local ITZ" obtained by the SEM/BSE method can neither describe the microstructure characteristics of the "complete ITZ" nor reflect the local variations between units around aggregates/sands.

(3) Statistical results show that the increase in porosity within the ITZ is minimal. The highly enhanced porosity (up to 30%), especially within the innermost strip, was not found in this study. The largest porosity differences between cement paste and innermost strip around aggregates and coarse sand were 1.60% and 0.53%, respectively.

(4) The porosity distributions of the ITZ around aggregate and coarse sand varied. The porosity of the innermost strip decreased with a decrease in the inclusion size (aggregate–coarse sand–fine sand).

Author Contributions: J.S.: Conceptualization, Data curation, Formal analysis, Investigation, Methodology, Writing—original draft. P.Q.: Funding acquisition, Methodology, Supervision, Writing—review and editing. Y.W.: Data curation, Formal analysis. All authors have read and agreed to the published version of the manuscript.

Funding: This research was funded by Open Research Fund Program of the State Key Laboratory of Hydroscience and Engineering (sklhse-KF-2025-D-06), the National Natural Science Foundation of China (52204094) and the National Key Research and Development Program of China (2023YFC3707803).

Data Availability Statement: Data will be made available on request.

Conflicts of Interest: Author Yunke Wang was employed by the company Sichuan Huaneng Kangding Hydropower. The remaining authors declare that the research was conducted in the absence of any commercial or financial relationships that could be construed as a potential conflict of interest.

References

1. Scrivener, K.L.; Bentur, A.; Pratt, P.L. Quantitative Characterization of the Transition Zone in High Strength Concretes. *Adv. Cem. Res.* **1988**, *1*, 230–237. [CrossRef]
2. Monteiro, P.J.M.; Maso, J.C.; Ollivier, J.P. The Aggregate-mortar Interface. *Cem. Concr. Res.* **1985**, *15*, 953–958. [CrossRef]
3. Kjellsen, K.O.; Wallevik, O.H.; Fjällberg, L. Microstructure and Microchemistry of the Paste-aggregate Interfacial Transition zone of High-performance Concrete. *Adv. Cem. Res.* **1998**, *10*, 33–40. [CrossRef]
4. Bentur, A.; Alexander, M.G. A Review of the Work of the RILEM TC 159-ETC: Engineering of the Interfacial Transition Zone in Cementitious Composites. *Mater. Struct.* **2000**, *33*, 82–87. [CrossRef]
5. Bentz, D.P.; Garboczi, E.J.; Stutzman, P.E. Computer Modelling of the Interfacial Transition Zone in Concrete. In *Interfkces in Cementitious Conlposites*; E & FN Spon: London, UK, 1993; pp. 107–116.
6. Houst, Y.F.; Sadouki, H.; Wittmann, F.H. Influence of aggregate concentration on the diffusion of CO_2 and O_2. In *Interfaces in Cementitious Composites RILEM Proceedings*; E & FN Spon: London, UK, 1993; pp. 279–288.
7. Halamickova, P.; Detwiler, R.J.; Bentz, D.P.; Garboczi, E.J. Water permeability and chloride ion diffusion in portland cement mortars: Relationship to sand content and critical pore diameter. *Cem. Concr. Res.* **1995**, *25*, 790–802. [CrossRef]
8. Yang, Z.; Ren, W.; Sharma, R.; McDonald, S.; Mostafavi, M.; Vertyagina, Y.; Marrow, T.J. In-situ X-ray computed tomography characterization of 3D fracture evolution and image-based numerical homogenization of concrete. *Cem. Concr. Compos.* **2017**, *75*, 74–83. [CrossRef]
9. Skarżyński, L.; Nitka, M.; Tejchman, J. Modelling of concrete fracture at aggregate level using FEM and DEM based on X-ray μCT images of internal structure. *Eng. Fract. Mech.* **2015**, *147*, 13–35. [CrossRef]
10. Königsberger, M.; Pichler, B.; Hellmich, C. Micromechanics of ITZ-Aggregate Interaction in Concrete Part II: Strength Upscaling. *J. Am. Ceram. Soc.* **2014**, *97*, 543–551.
11. Shahbazi, S.; Rasoolan, I. Meso-scale finite element modeling of non-homogeneous three-phase concrete. *Case Stud. Constr. Mater.* **2017**, *6*, 29–42. [CrossRef]
12. Akçaoğlu, T.; Tokyay, M.; Çelik, T. Assessing the ITZ microcracking via scanning electron microscope and its effect on the failure behavior of concrete. *Cem. Concr. Res.* **2005**, *35*, 358–363. [CrossRef]
13. Chang, H.; Feng, P.; Lyu, K.; Liu, J. A novel method for assessing C-S-H chloride adsorption in cement pastes. *Constr. Build. Mater.* **2019**, *225*, 324–331.
14. Wang, P.; Jia, Y.; Li, T.; Hou, D.; Zheng, Q. Molecular dynamics study on ions and water confined in the nanometer channel of Friedel's salt: Structure dynamics and interfacial interaction. *Phys. Chem. Chem. Phys.* **2018**, *20*, 27049–27058. [CrossRef] [PubMed]
15. Sun, Z.; Garboczi, E.J.; Shah, S.P. Modeling the elastic properties of concrete composites. *Cem. Concr. Compos.* **2007**, *29*, 22–28. [CrossRef]
16. Zheng, J.; Lu, J.; Wu, Z. Prediction of the elastic modulus of concrete with inhomogeneous ITZ. *Acta Mater. Compos. Sin.* **2007**, *29*, 22–38.
17. Hashin, Z.; Monteiro, P.J.M. An inverse method to determine the elastic properties of the interphase between the aggregate and the cement paste. *Cem. Concr. Res.* **2002**, *32*, 1291–1300. [CrossRef]
18. Zhang, P.; Lei, D.; Ren, Q.; He, J.; Shen, H.; Yang, Z. Experimental and numerical investigation of debonding process of the FRP plate-concrete interface. *Constr. Build. Mater.* **2020**, *235*, 117457. [CrossRef]
19. Scrivener, K.L. Microstructure of Concrete. *Mater. Sci. Concr. III* **1989**, *I*, 127.
20. Diamond, S. Considerations in Image Analysis as Applied to Investigations of the ITZ in Concrete. *Cem. Concr. Compos.* **2001**, *23*, 171–178. [CrossRef]
21. Diamond, S.; Huang, J. The ITZ in Concrete-A Different View based on Image Analysis and SEM Observations. *Cem. Concr. Compos.* **2001**, *23*, 179–188. [CrossRef]

22. Scrivener, K.L. Backscattered Electron Imaging of Cementitious Microstructures: Understanding and Quantification. *Cem. Concr. Compos.* **2004**, *26*, 935–945. [CrossRef]
23. Lyu, K.; She, W.; Miao, C.; Chang, H.; Gu, Y. Quantitative characterization of pore morphology in hardened cement paste via SEMBSE image analysis. *Constr. Build. Mater.* **2019**, *202*, 589–602. [CrossRef]
24. Larbi, J.A. Microstructure of the interfacial zone around aggregate particles in concrete. *NASA STI/Recon Tech. Rep. N* **1993**, *94*, 19322.
25. Zhu, Z.; Chen, H. Overestimation of ITZ thickness around regular polygon and ellipse aggregate. *Comput. Struct.* **2017**, *182*, 205–218. [CrossRef]
26. Head, M.K.; Wong, H.S.; Buenfeld, N.R. Characterising aggregate surface geometry in thin-sections of mortar and concrete. *Cem. Concr. Res.* **2008**, *38*, 1227–1231. [CrossRef]
27. Ollivier, J.P.; Maso, J.C.; Bouordette, B. Interfacial transition zone in concrete. *Adv. Cem. Based Mater.* **1995**, *2*, 30–38. [CrossRef]
28. Scrivener, K. The interfacial transition zone (ITZ) between cement paste and aggregate in concrete. *Interface Sci.* **2004**, *12*, 411–421. [CrossRef]
29. Jia, Z.; Han, Y.; Zhang, Y.; Qiu, C.; Hu, C.; Li, Z. Quantitative characterization and elastic properties of Interfacial Transition Zone around coarse aggregate in concrete. *J. Wuhan Univ. Technol.-Mater. Sci. Ed.* **2017**, *32*, 838–844. [CrossRef]
30. Newman, J.; Owens, P. Properties of lightweight concrete. In *Advanced Concrete Technology*; Woodhead Publishing Limited: Cambridge, UK, 2003.
31. Rangaraju, P.R.; Olek, J.; Diamond, S. An investigation into the influence of inter-aggregate spacing and the extent of the ITZ on properties of Portland cement concrete. *Cem. Concr. Res.* **2010**, *40*, 1601–1608. [CrossRef]
32. Shi, Y.; Lv, X.; Zhou, S.; Liu, Z.A.; Yang, M.; Liu, C.; Lu, C. Mechanical properties; durability, and ITZ characteristics of full-grade dam concrete prepared by aggregates with surface rust stains. *Constr. Build. Mater.* **2021**, *305*, 124798. [CrossRef]
33. Nežerka, V.; Bílý, P.; Hrbek, V.; Fládr, J. Impact of silica fume, fly ash, and metakaolin on the thickness and strength of the ITZ in concrete. *Cem. Concr. Compos.* **2019**, *103*, 252–262. [CrossRef]
34. Gao, J.M.; Qian, C.X.; Liu, H.F.; Wang, B.; Li, L. ITZ microstructure of concrete containing GGBS. *Cem. Concr. Res.* **2005**, *35*, 1299–1304. [CrossRef]
35. Bentz, D.P.; Hwang, J.T.G.; Hagwood, C.; Garboczi, E.J.; Snyder, K.A.; Buenfeld, N.; Scrivener, K.L. Interfacial zone percolation in concrete: Effects of interfacial zone thickness and aggregate shape. In *Microstructure of Cement-Based Systems/Bonding and Interfaces in Cementitious Systems*; Diamond, S., Mindess, S., Glasser, F.P., Roberts, L.W., Skalny, J.P., Wakeley, L.D., Eds.; Materials Research Society Symposium Proceedings; Materials Research Society: Pittsburgh, PA, USA, 1995; Volume 370, pp. 437–442.
36. Lyu, K.; She, W. Determination of aggregate surface morphology at the Interfacial Transition zone (ITZ). *J. Vis. Exp.* **2019**, *154*, e60245. [CrossRef]
37. Huang, J. Microstructural Study of the Interfacial Transition Zone in Concrete Using Backscatter Mode Scanning Electron Microscopy with Image Analysis. Ph.D. thesis, Purdue University, West Lafayette, IN, USA, 1998.
38. Li, S.; Chen, G.; Ji, G.; Lu, Y. Quantitative damage evaluation of concrete suffered freezing–thawing by DIP technique. *Constr. Build. Mater.* **2014**, *69*, 177–185. [CrossRef]
39. Li, S.G.; Lu, Y.H.; Chen, G.X. Quantitative damage evaluation of AAR-affected concrete by DIP technique. *Mag. Concr. Res.* **2013**, *65*, 321–330. [CrossRef]
40. Broekmans, M.A.; Fernandes, I.; Fredin, O.; Margreth, A. Polarization-fluorescence microscopy in the study of aggregate and concrete. *Elem. Int. Mag. Mineral. Geochem. Petrol.* **2022**, *18*, 321–326. [CrossRef]
41. Ammouche, A.; Breysse, D.; Hornain, H.; Didry, O.; Marchand, J. A new image analysis technique for the quantitative assessment of microcracks in cement-based materials. *Cem. Concr. Res.* **2000**, *1*, 25–35. [CrossRef]
42. Litorowicz, A. Identification and quantification of cracks in concrete by optical fluorescent microscopy. *Cem. Concr. Res.* **2006**, *8*, 1508–1515. [CrossRef]
43. Wang, S.G.; Shen, J.R.; Mu, P.Y. Effect of natural crack distributions on coal failure process based on fluorescent epoxy impregnation method and phase-field FEM simulation. *Bull. Eng. Geol. Environ.* **2023**, *82*, 304. [CrossRef]
44. Shen, J.; Li, W.; Xu, Q.; Wang, S.; Qian, P. Initial Microcrack Characteristics of Concrete Interfacial Transition Zone and Cement Paste. *J. Mater. Civ. Eng.* **2023**, *35*, 04023446. [CrossRef]
45. Shen, J.; Wang, S.; Qian, P.; Liu, Y.; Chen, Y. Experimental research on microstructure characteristics and mechanical performance of interfaces between concrete layers. *Front. Mater.* **2025**, *12*, 1576065. [CrossRef]
46. Gran, H.C. Fluorescent liquid replacement technique–a means of crack detection and water: Binder ratio determination in high strength concretes. *Cem. Concr. Res.* **1995**, *25*, 1063–1074. [CrossRef]
47. Diamond, S. Measurement of the viscosity of resin used in SEM specimen preparation. *Mater. Struct.* **2007**, *40*, 995–1000.
48. Preibisch, S.; Saalfeld, S.; Tomancak, P. Globally optimal stitching of tiled 3D microscopic image acquisitions. *Bioinformatics* **2009**, *25*, 1463–1465. [CrossRef] [PubMed]

49. Diamond, S.; Huang, J. The interfacial transition zone: Reality or myth? In *Interfacial Transition Zone in Cementitious Composites*; E & FN Spon: London, UK, 1998; pp. 1–40.
50. Mehta, P.K.; Monteiro, P.J.M. *Concrete: Microstructure, Properties, and Materials*, 4th ed.; McGraw-Hill Education: New York, NY, USA, 2014.
51. Nilson, A.J.; Monteiro, P.J.M. Concrete: A three phase material. *Cem. Concr. Res.* **1993**, *23*, 147–151. [CrossRef]
52. Lee, K.M.; Park, J.H. A numerical model for elastic modulus of concrete considering interfacial transition zone. *Cem. Concr. Res.* **2008**, *38*, 396–402. [CrossRef]
53. LeRoy, R.; deLarrard, F. A discussion on the paper "Concrete: A three phase material" by A.U. Nilsen and P.J.M. Monteiro. *Cem. Concr. Res.* **1994**, *24*, 189–193.

Disclaimer/Publisher's Note: The statements, opinions and data contained in all publications are solely those of the individual author(s) and contributor(s) and not of MDPI and/or the editor(s). MDPI and/or the editor(s) disclaim responsibility for any injury to people or property resulting from any ideas, methods, instructions or products referred to in the content.